

A new formulation for coupled magma/mantle dynamics

Juliane Dannberg¹, Rene Gassm  ller¹, Ryan Grove², Timo Heister³

¹ *University of California, Davis; judannberg@gmail.com and rene.gassmoeller@mailbox.org*

² *Mathematical Sciences, Clemson University; rrgrove6@gmail.com*

³ *Scientific Computing and Imaging Institute, University of Utah; heister@sci.utah.edu*

SUMMARY

Many open problems in the Earth sciences can only be understood by modelling the porous flow of melt through a viscously deforming solid rock matrix. However, the system of equations describing this process becomes mathematically degenerate in the limit of vanishing melt fraction. Numerical methods that do not consider this degeneracy or avoid it solely by regularising specific material properties generally become computationally expensive as soon as the melt fraction approaches zero in some part of the domain.

Here, we present a new formulation of the equations for coupled magma/mantle dynamics that addresses this problem, and allows it to accurately compute large-scale 3-D magma/mantle dynamics simulations with extensive regions of zero melt fraction. We achieve this by rescaling one of the solution variables, the compaction pressure, which ensures that for vanishing melt fraction, the equation causing the degeneracy becomes an identity and the other two equations revert to the Stokes system. This allows us to split the domain into two parts: In mesh cells where melt is present, we solve the coupled system of magma/mantle dynamics. In cells without melt, we solve the Stokes system as it is done for mantle convection without melt transport and constrain the remaining degrees of freedom.

We have implemented this formulation in the open source geodynamic modelling code

ASPECT and illustrate the improved performance compared to the previous three-field formulation, showing numerically that the new formulation is optimal in terms of problem size and only minimally sensitive to model parameters. Beyond that, we demonstrate the applicability to realistic problems by showing large-scale 2-D and 3-D models of mid-ocean ridges with complex rheology. Hence, we believe that our new formulation and its implementation in ASPECT will prove a valuable tool for studying the interaction of melt segregating through and interacting with a solid host rock in the Earth and other planetary bodies using high-resolution, three-dimensional simulations.

Key words: Numerical solutions, Dynamics of lithosphere and mantle, Magma migration and fragmentation, Mechanics, theory, and modelling, Mid-ocean ridge processes

1 INTRODUCTION

Many Earth system processes are controlled by the porous flow of melt through a viscously deforming solid rock matrix. The equations that describe this process have been derived a long time ago (e.g. McKenzie 1984): The motion of the solid is governed by Stokes flow, and the melt is transported according to Darcy’s law. A large number of numerical models have been formulated that use these equations for different application cases (e.g. Katz 2006, 2008; Weatherley & Katz 2012; Keller et al. 2013; Turner et al. 2017; Butler 2017; Keller et al. 2017; Katz et al. 2017). However, many formulations of coupled Stokes/Darcy flow break down in the limit of vanishing melt fraction (or porosity) because for this case the system is mathematically degenerate (Arbogast et al. 2017).

A common solution for this problem is introducing a cutoff or regularization for certain material properties or solution variables (Keller et al. 2013; Rhebergen et al. 2015; Wilson et al. 2014; Dannberg & Heister 2016). Regularising the equations in such a way generally means that the system does not exactly reduce to the Stokes problem in the case of zero porosity. Beyond that, Arbogast et al. (2017) find that numerical methods that do not take into account the degeneracy of the porosity ϕ , and instead regularize the equations for example by imposing a small non-zero porosity everywhere, are sure to have a condition number that grows as the porosity approaches zero. This makes it computationally expensive to compute numerical models with regions of vanishing porosity.

Arbogast et al. (2017) address this problem by developing a mixed variational framework, carefully scaling the Darcy variables by powers of the porosity, and defining a mixed finite element method for solving the Darcy–Stokes system. This method has the drawback that it requires a particular choice of finite elements, and that it is based on specific assumptions on how material properties like the per-

meability and the bulk viscosity depend on the amount of melt present. In addition, the method has not been tested on realistic large-scale, 3-D application models or in parallel computations.

Here, we present a new, more general formulation of the equations for coupled Stokes/Darcy flow that addresses these shortcomings, and allows it to compute large-scale 3-D magma/mantle dynamics simulations with extensive regions of zero porosity. We have implemented this formulation in the open source geodynamic modelling code ASPECT (Heister et al. 2017; Dannberg & Heister 2016; Bangerth et al. 2018b,a), which is based on the deal.II finite element library (Bangerth et al. 2007; Alzetta et al. 2018, accepted). Using ASPECT, we have tested the new method on real-world applications, in parallel, and with adaptive mesh refinement.

In the following, we will derive our new formulation and its numerical implementation, and discuss the convergence behaviour that is expected for this method (Section 2). We will demonstrate the correctness of our implementation based on a benchmark case that specifically addresses the boundary between regions with and without melt, and illustrate the improved performance compared to the three-field formulation used in Dannberg & Heister (2016) (Section 3.1). Finally, we will show 2-D and 3-D mid-ocean ridge models to demonstrate the applicability of our method to earth-like settings (Section 3.2 and 3.3). The code used to generate these results can be found in the repository at <https://github.com/geodynamic/aspect> and all input files to reproduce the results are available at <https://github.com/tjhei/paper-aspect-melt-paper-2-data>.

2 FORMULATION OF THE PROBLEM

We consider the equations describing the behaviour of silicate melt percolating through and interacting with a viscously deforming host rock (e.g. McKenzie 1984):

$$\frac{\partial}{\partial t} [\rho_f \phi] + \nabla \cdot [\rho_f \phi \mathbf{u}_f] = \Gamma, \quad (1)$$

$$\frac{\partial}{\partial t} [\rho_s (1 - \phi)] + \nabla \cdot [\rho_s (1 - \phi) \mathbf{u}_s] = -\Gamma, \quad (2)$$

$$\phi (\mathbf{u}_f - \mathbf{u}_s) = -K_D (\nabla p_f - \rho_f \mathbf{g}), \quad (3)$$

$$-\nabla \cdot [2\eta \dot{\epsilon} + \xi (\nabla \cdot \mathbf{u}_s) \mathbf{1}] + \nabla p_f = \bar{\rho} \mathbf{g}. \quad (4)$$

Here, ϕ is the porosity, ρ is the density, \mathbf{u} is the velocity, Γ is the melting rate, K_D is the Darcy coefficient, p is the pressure, \mathbf{g} is the gravity vector, η is the shear viscosity, ξ is the bulk viscosity and $\dot{\epsilon} = \nabla \mathbf{u}_s + (\nabla \mathbf{u}_s)^T - \frac{1}{3} (\nabla \cdot \mathbf{u}_s) \mathbf{1}$ is the strain rate. The index f indicates the melt (fluid), the index s indicates the solid, and quantities that are averaged between the solid and the fluid are denoted by a bar.

Two important material properties in the context of the transition between solid-state mantle convection and two-phase magma/mantle dynamics are K_D and ξ . The Darcy coefficient is defined as the ratio of permeability k and fluid viscosity η_f , and while η_f is often, for simplicity, assumed to be constant, the permeability depends on the porosity as $k \propto \phi^2$ or $k \propto \phi^3$. This means that for vanishing porosity, $K_D = 0$. The compaction viscosity ξ is often assumed to scale as $\xi \propto \phi^{-1}$, so that the matrix can not be compacted ($\xi \rightarrow \infty$) if no melt is present.

2.1 Original formulation used in Dannberg & Heister (2016)

In previous work (Dannberg & Heister 2016), we reformulated the equations by building on the three-field formulation from Keller et al. (2013), extending them to compressible solid and fluid phases:

$$\begin{aligned}
 & -\nabla \cdot (2\eta\dot{\epsilon}) + \nabla p_f + \nabla p_c = \bar{\rho}\mathbf{g}, \\
 & \nabla \cdot \mathbf{u}_s \left[-\nabla \cdot K_D \nabla p_f - K_D \nabla p_f \cdot \frac{\nabla \rho_f}{\rho_f} \right] = \left[-\nabla \cdot (K_D \rho_f \mathbf{g}) \right. \\
 & \quad \left. + \Gamma \left(\frac{1}{\rho_f} - \frac{1}{\rho_s} \right) \right. \\
 & \quad \left. - \frac{\phi}{\rho_f} \mathbf{u}_s \cdot \nabla \rho_f \right] - (\mathbf{u}_s \cdot \mathbf{g})(1 - \phi)\kappa_s \rho_s \\
 & \quad \left[-K_D \mathbf{g} \cdot \nabla \rho_f \right], \\
 & \nabla \cdot \mathbf{u}_s + \frac{p_c}{\xi} = 0.
 \end{aligned}$$

All terms that vanish in the limit of zero porosity and no melting are highlighted. These equations can then be brought into the weak form (see Dannberg & Heister 2016) and solved as outlined in Rhebergen et al. (2015). This results in the linear system:

$$\begin{pmatrix} \mathbf{A} & \mathbf{B}^T & \mathbf{B}^T \\ \mathbf{B} & \mathbf{N} & \mathbf{0} \\ \mathbf{B} & \mathbf{0} & \mathbf{K} \end{pmatrix} \begin{pmatrix} \mathbf{U}_s \\ \mathbf{P}_f \\ \mathbf{P}_c \end{pmatrix} = \begin{pmatrix} \mathbf{F} \\ \mathbf{G} \\ \mathbf{0} \end{pmatrix}. \quad (5)$$

\mathbf{A} , \mathbf{B} , \mathbf{N} , \mathbf{K} , \mathbf{F} and \mathbf{G} are defined as in Dannberg & Heister (2016). For a more extensive discussion of these matrix blocks, we refer the reader to Equation (12).

While this formulation allows it to run large-scale, 3-D models of coupled magma/mantle dynamics, it has several shortcomings: The number of linear solver iterations increases with an increasing ratio of compaction viscosity ξ and shear viscosity η , which corresponds to a decreasing porosity ϕ . In addition, for the limit of $\phi \rightarrow 0$ (which implies $\sqrt{K_D} \rightarrow 0$), the compaction pressure p_c is not defined, because $\xi \rightarrow \infty$ (the compaction viscosity is generally assumed to scale as $\xi \propto \phi^{-1}$, at least

if the model is incompressible, which implies that $-(\mathbf{u}_s \cdot \mathbf{g})(1 - \phi)\kappa_s \rho_s = 0$). In this case, the last two equations become linearly dependent (and the whole system is ill-posed), which is also the reason for the increasing number of linear solver iterations that are needed for decreasing porosity values. Indeed, Arbogast et al. (2017) note that all numerical methods that do not specifically take into account the degeneracy of the porosity are sure to have a condition number that grows as the porosity approaches zero.

In addition, this means that in order to solve the system in spite of this problem, some limit has to be imposed on the compaction viscosity, either in form of a minimum value, or in form of a regularization term that is added to the compaction pressure equation. While this form of stabilization allows it to solve the equations, the system will not revert to the incompressible one-phase Stokes equations for vanishing porosity, as there will always be a non-zero contribution of the compaction term that is needed to stabilize the system.

2.2 New formulation

To address these problems, we have developed a new formulation based on the ideas presented in Arbogast et al. (2017). We replace p_c by \bar{p}_c , using the relation $p_c = \sqrt{K'_D} \bar{p}_c$, where K'_D is the Darcy coefficient, but rescaled to a reference value representative of the model (for details, see Section 2.3). To keep the matrix symmetric, we also scale the last equation by $\sqrt{K'_D}$, and arrive at the following, new system of partial differential equations:

$$\begin{aligned}
 & -\nabla \cdot (2\eta \dot{\epsilon}) + \nabla p_f + \nabla \left(\sqrt{K'_D} \bar{p}_c \right) = \bar{\rho} \mathbf{g}, \\
 & \nabla \cdot \mathbf{u}_s \left[-\nabla \cdot K_D \nabla p_f - K_D \nabla p_f \cdot \frac{\nabla \rho_f}{\rho_f} \right] = \left[-\nabla \cdot (K_D \rho_f \mathbf{g}) \right. \\
 & \quad \left. + \Gamma \left(\frac{1}{\rho_f} - \frac{1}{\rho_s} \right) \right. \\
 & \quad \left. - \frac{\phi}{\rho_f} \mathbf{u}_s \cdot \nabla \rho_f \right] - (\mathbf{u}_s \cdot \mathbf{g})(1 - \phi)\kappa_s \rho_s \\
 & \quad \left[-K_D \mathbf{g} \cdot \nabla \rho_f \right], \\
 & \sqrt{K'_D} \nabla \cdot \mathbf{u}_s + \frac{K'_D \bar{p}_c}{\xi} = 0.
 \end{aligned}$$

Again, terms that vanish in the limit of zero porosity are marked in gray boxes. For this new formulation, it becomes apparent that for the limit of $\phi \rightarrow 0$, the last equation vanishes completely and we

recover the Stokes system from the first two equations, as $\nabla(\sqrt{K'_D}\bar{p}_c) \rightarrow 0$.

$$\begin{aligned} -\nabla \cdot (2\eta\dot{\epsilon}) + \nabla p_f &= \bar{\rho}\mathbf{g}, \\ \nabla \cdot \mathbf{u}_s &= -(\mathbf{u}_s \cdot \mathbf{g})\kappa_s\rho_s. \end{aligned}$$

In contrast to the original formulation, the real compaction pressure p_c is now defined everywhere, as it is computed as $p_c = \sqrt{K'_D}\bar{p}_c$. So for the case of vanishing melt fraction $\phi = 0$, which implies $\sqrt{K'_D} = 0$, this scaling always leads to $p_c = 0$. While the (rescaled) compaction pressure \bar{p}_c is still not defined in this limit, it is also not used anywhere in the system. Hence, to make sure that the linear system can be solved, we can constrain these degrees of freedom in regions where the porosity is below a given threshold to $\bar{p}_c = 0$. An example for this is given in Figure 1. Beyond that, this formulation has the advantage that no additional computational resources are used to solve the coupled Stokes/Darcy system if no melt is present.

Solving the single phase Stokes system if the porosity is below a given threshold can also be motivated physically: When solid rock starts to melt, melt is expected to form in isolated patches between the mineral grains. Melt segregation and compaction only start to occur once the porosity reaches a critical value – the percolation threshold – and pockets of melt become interconnected (e.g. Zhu & Hirth 2003; Cheadle et al. 2004). In other words, the permeability of the rock is zero, and there is no relative movement between the phases, until a given porosity is reached. Below that percolation threshold, the motion of the rock can be described accurately by single phase Stokes flow. As the critical porosity is influenced by grain size, composition, and other properties of the rock, it can be chosen as a model input parameter.

In the incompressible formulation, which is a good approximation for models that do not span a large depth range and is commonly used for these applications, all terms that contain the solid compressibility or the fluid density gradient vanish:

$$-\nabla \cdot (2\eta\dot{\epsilon}) + \nabla p_f + \nabla(\sqrt{K'_D}\bar{p}_c) = \bar{\rho}\mathbf{g}, \quad (6)$$

$$\begin{aligned} \nabla \cdot \mathbf{u}_s - \nabla \cdot K_D \nabla p_f &= -\nabla \cdot (K_D \rho_f \mathbf{g}) \\ &+ \Gamma \left(\frac{1}{\rho_f} - \frac{1}{\rho_s} \right), \end{aligned} \quad (7)$$

$$\sqrt{K'_D} \nabla \cdot \mathbf{u}_s + \frac{K'_D \bar{p}_c}{\xi} = 0. \quad (8)$$

The weak form of the full problem is given by: Find \mathbf{u}_s, p_f, p_c with

$$(2\eta\dot{\varepsilon}(\mathbf{u}_s), \dot{\varepsilon}(\mathbf{v}_s)) - \left(\frac{2}{3}\eta\nabla \cdot \mathbf{u}_s, \nabla \cdot \mathbf{v}_s\right) - (p_f, \nabla \cdot \mathbf{v}_s) - (\sqrt{K'_D}\bar{p}_c, \nabla \cdot \mathbf{v}_s) = (\bar{\rho}\mathbf{g}, \mathbf{v}_s), \quad (9)$$

$$\begin{aligned} & -(\nabla \cdot \mathbf{u}_s, q_f) - (K_D \nabla p_f, \nabla q_f) \\ & + \left(K_D \nabla p_f \cdot \frac{\nabla \rho_f}{\rho_f}, q_f\right) = -(K_D \rho_f \mathbf{g}, \nabla q_f) \\ & + \int_{\partial\Omega} q_f K_D (\rho_f \mathbf{g} - \mathbf{f}_2) \cdot \vec{n} \, ds \\ & - \left(\frac{1}{\rho_f} - \frac{1}{\rho_s}\right) (\Gamma, q_f) \\ & + \left(\frac{\phi}{\rho_f} \mathbf{u}_s \cdot \nabla \rho_f, q_f\right) \\ & + ((\mathbf{u}_s \cdot \mathbf{g})(1 - \phi) \kappa_s \rho_s, q_f) \\ & + (K_D \mathbf{g} \cdot \nabla \rho_f, q_f), \end{aligned} \quad (10)$$

$$-\left(\sqrt{K'_D} \nabla \cdot \mathbf{u}_s, q_c\right) - \left(\frac{1}{\xi} K'_D \bar{p}_c, q_c\right) = 0. \quad (11)$$

for all test functions \mathbf{v}_s, q_f, q_c .

Note that we have made the assumption that at the interface $\partial\Omega_{\text{melt}}$ between regions where the compaction pressure is constrained to $p_c = 0$ and the regions where we solve for the full two-phase system, $\nabla p_f = \rho_f \mathbf{g}$. This follows from integration by parts of Equation (7), which yields

$$\begin{aligned} & -(\nabla \cdot \mathbf{u}_s, q_f) - (K_D \nabla p_f, \nabla q_f) = -(K_D \rho_f \mathbf{g}, \nabla q_f) - \left(\frac{1}{\rho_f} - \frac{1}{\rho_s}\right) (\Gamma, q_f) \\ & + \int_{\partial\Omega_{\text{melt}}} q_f K_D (\rho_f \mathbf{g} - \nabla p_f) \cdot \vec{n} \, ds \end{aligned}$$

for the interface $\partial\Omega_{\text{melt}}$. As $K_D = 0$ in the cells without melt, and $K_D > 0$ in the cells where melt is present, $\int_{\partial\Omega_{\text{melt}}} (\rho_f \mathbf{g} - \nabla p_f) \cdot \vec{n} \, ds = 0$. Because of Darcy's law (Equation 3), this condition is equivalent to the assumption that the melt velocity equals the solid velocity at the interface between the two regions.

This means we have to solve the linear system:

$$\begin{pmatrix} \mathbf{A} & \mathbf{B}^T & \sqrt{K'_D} \mathbf{B}^T \\ \mathbf{B} & \mathbf{N} & \mathbf{0} \\ \sqrt{K'_D} \mathbf{B} & \mathbf{0} & K'_D \mathbf{K} \end{pmatrix} \begin{pmatrix} \mathbf{U}_s \\ \mathbf{P}_f \\ \bar{\mathbf{P}}_c \end{pmatrix} = \begin{pmatrix} \mathbf{F} \\ \mathbf{G} \\ \mathbf{0} \end{pmatrix}, \quad (12)$$

where \mathbf{A} is the discretization of $(2\eta\dot{\varepsilon}(\mathbf{u}_s), \dot{\varepsilon}(\mathbf{v}_s)) - (\frac{2}{3}\eta\nabla \cdot \mathbf{u}_s, \nabla \cdot \mathbf{v}_s)$, \mathbf{B} is given by $-(p_f, \nabla \cdot \mathbf{v}_s)$, \mathbf{F} is given by $(\bar{\rho}\mathbf{g}, \mathbf{v}_s)$, \mathbf{N} is given by $-(K_D \nabla p_f, \nabla q_f)$ in the incompressible case, \mathbf{G} is given by $-(K_D \rho_f \mathbf{g}, \nabla q_f) + \int_{\partial\Omega} q_f K_D (\rho_f \mathbf{g} - \mathbf{f}_2) \cdot \vec{n} \, ds - \left(\frac{1}{\rho_f} - \frac{1}{\rho_s}\right) (\Gamma, q_f)$ in the incompressible case, and

\mathbf{K} is given by $-\left(\frac{1}{\xi}\bar{p}_c, q_c\right)$. For compressible computations, \mathbf{N} also contains the non-symmetric, third term from (10), and \mathbf{G} contains the remaining terms on the right-hand side of (10), which contain κ_s and $\nabla\rho_f$.

As the block structure of the linear system remains the same as in Dannberg & Heister (2016), the same solver strategy, based on Rhebergen et al. (2015), can be employed to solve the block system (12). Specifically, we use flexible GMRES with the block preconditioner (preconditioned from the right):

$$\mathbf{P}^{-1} = \begin{pmatrix} \mathbf{A} & \mathbf{B}^T & \sqrt{K'_D}\mathbf{B}^T \\ \mathbf{0} & -\frac{1}{\eta}\mathbf{M}_{p_f} - K_D\mathbf{L}_{p_f} & -\frac{\sqrt{K'_D}}{\eta}\mathbf{M}_{p_f,p_c} \\ \mathbf{0} & -\frac{\sqrt{K'_D}}{\eta}\mathbf{M}_{p_c,p_f} & -K'_D\left(\frac{1}{\eta} + \frac{1}{\xi}\right)\mathbf{M}_{p_c} \end{pmatrix}^{-1}.$$

\mathbf{M}_* and \mathbf{L}_* are mass and stiffness matrices, respectively. \mathbf{A}^{-1} is approximated using an inner CG solver preconditioned by Trilinos ML applied to the diagonal blocks of \mathbf{A} . The Schur complement solves for the bottom-right 2 by 2 block are also done using CG preconditioned by Trilinos ML.

2.3 Constraining the compaction pressure DoFs

As outlined in Section 2.2, we constrain the compaction pressure degrees of freedom to $\bar{p}_c = 0$ in regions where the porosity is below a given threshold. In practice, we choose this threshold $K_{\text{threshold}}$ based on the Darcy coefficient K_D relative to a reference value K_{D_0} , as this ratio is what we use to rescale the different matrix blocks in the linear system (12). K_{D_0} is defined as the ratio of permeability and fluid viscosity at a porosity that is typical for the model (in the following examples, we will use a value of 1%), but because it is part of ASPECT’s ‘material model’ plugin structure (see Bangerth et al. 2018b) it can be chosen in dependence of the specific application case. This means that the last equation in (12) will not be rescaled at all if the porosity equals this reference porosity.

The decision to constrain degrees of freedom is made for each cell, separating the model domain into ‘melt cells’, where the full equations are solved, and cells that are not ‘melt cells’ with the compaction pressure degrees of freedom being constrained. An example for this is shown in Figure 1. A cell is determined to be a ‘melt cell’ if $K_D/K_{D_0} > K_{\text{threshold}}$ on any of the quadrature points. The default value is given by $K_{\text{threshold}} = 10^{-3}$, but it is an input parameter that can be chosen differently in each model (for its influence on solver performance, see Section 3.2.5). Based on this evaluation, a scaling factor $\sqrt{K'_D}$ for the compaction pressure is computed for each cell. In melt cells, $K'_D = \max(K_{D_{\text{mean}}}/K_{D_0}, K_{\text{threshold}})$, where $K_{D_{\text{mean}}}$ is the geometric mean of the Darcy coefficient for the respective cell. Providing a minimum value for the scaling factor guarantees that we avoid the mathematically degenerate region in all quadrature points where we solve the two-phase flow equa-

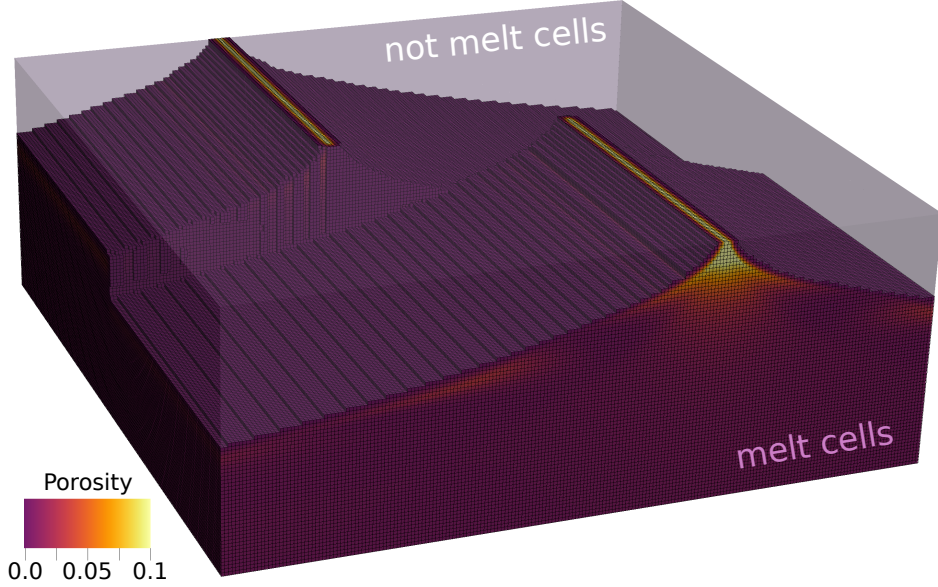


Figure 1. Distribution of melt cells and cells that are not melt cells in a 3-D model of a transform fault. The coupled Stokes–Darcy equations are only solved in cells where the porosity is above a given threshold.

tions. In cells that are not melt cells, we set $K'_D = 0$, and all compaction pressure degrees of freedom are constrained to zero. Effectively, this removes the equations for \bar{p}_c in the Stokes region and for a computation without any melt cells, the linear system and solver cost is effectively equivalent to a standard Stokes solver.

This algorithm is executed once in every time step, after solving the advection equation for the porosity, to make sure that the constraints for system (12) are the same for every nonlinear iteration and that the nonlinear solver converges. To compute the Darcy coefficient in Equation (10), the same threshold is applied: $K_D = \max(K_{D_{\text{mean}}}, K_{\text{threshold}} K_{D_0})$ in melt cells, and zero otherwise.

Dannberg & Heister (2016) used a different threshold to discriminate between model regions with and without melt migration, directly based on the porosity. In their method, the full two-phase flow equations are only solved for $\phi > \phi_{\text{threshold}}$. Both methods are compared for different threshold values in Section 3.2.5, and – assuming a reference porosity of 0.01 – both thresholds are related as $\phi_{\text{threshold}} = 0.01 K_{\text{threshold}}^{2/3}$.

2.4 Finite Element Formulation

Now we still require a choice of finite element spaces for the discrete solution $(\mathbf{u}_{s,h}, p_{f,h}, p_{c,h}) \in W_h \subset W = H_0^1(\Omega) \times H^1(\Omega) \times L^2(\Omega)$. This system is analysed in detail in (Grove 2017). We use quadrilateral cells and the following, typical polynomial finite element spaces: Let Q_k be the

definition	optimal rates for \mathbf{u}_s, p_f, p_c	$K_D = 0$	$K_D > 0$
$W_2 = Q_2^d \times Q_2 \times DGP_1$	3,3,2	unstable	3,3,2 (optimal)
$W_2^L = Q_2^d \times Q_1 \times DGP_1$	3,2,2	3,2,- (optimal)	2,2,1 (suboptimal)

Table 1. Different choices for finite element spaces. The columns contain the optimal convergence rates based on approximation quality of the element in the L2 norm, the expected convergence rates for a problem without melt, and for melt everywhere.

continuous space with tensor-product polynomials of degree k on each cell and let DGP_k be the discontinuous space with polynomials of degree k .

We choose Q_{k+1} for each component of the velocity $u_{s,h}$. To be able to solve for a discrete $p_{c,h}$ in (11), the space needs to be discontinuous to allow a jump from melt to a no-melt cell, so we choose DGP_k . For $p_{f,h}$ we have two sensible choices:

$$W_k = Q_{k+1}^d \times Q_{k+1} \times DGP_k \quad \text{or} \quad W_k^L = Q_{k+1}^d \times Q_k \times DGP_k,$$

namely choosing a higher or lower polynomial degree.

If we consider the case $K_D = 0$ (no melt in the domain), we recover the standard Stokes system and well-posedness requires a stable finite element choice for $\mathbf{u}_{s,h}$ and $p_{f,h}$ to guarantee convergence. One example is the usage of Taylor-Hood elements, where the velocity is discretized with one polynomial degree higher than the pressure like in the definition of W_k^L . This means W_k^L is stable and gives optimal convergence rates, while W_k is not a stable choice leading to oscillating solutions.

On the other hand, if we consider a situation with melt everywhere ($K_D \geq K_{D,\min} > 0$), both discrete spaces give stable solutions, but W_k^L gives suboptimal convergence rates, while W_k will achieve optimal rates provided the data and exact solution are sufficiently smooth. We note that the inverse of the minimum value of K_D appears in the stability estimate, confirming the issue of letting K_D go to zero.

We decided to do our computations with W_2^L , the lowest order discretization that gives stable solutions even for $K_D = 0$. Table 1 summarizes the discretization choices and convergence rates in $L_2(\Omega)$, and the convergence rates in Figure 3 confirm these estimates.

Alternatives would be to either always require a minimum K_D , add stabilization terms to make the Stokes solution stable for $K_D = 0$, or discretize with different finite element spaces in the regions with and without melt.

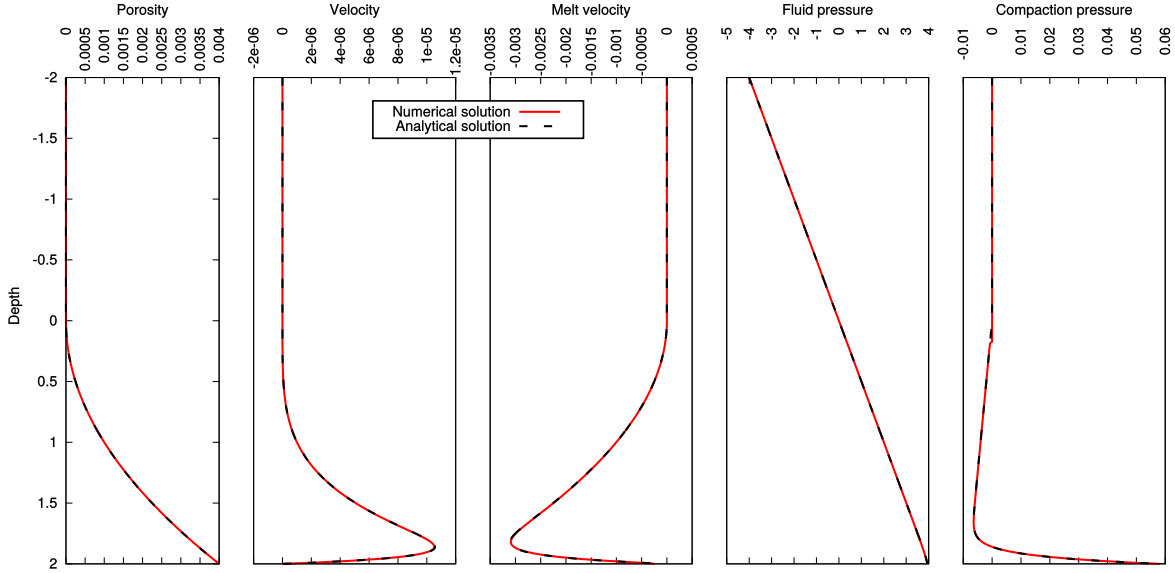


Figure 2. Setup of the benchmark given in Arbogast et al. (2017). The solution derived in Arbogast et al. (2017) is given as a dashed black line, and the solution computed numerically with ASPECT is marked by a red line.

3 RESULTS

3.1 1-D analytical solution for the interface between regions with and without melt

We use a 1-D benchmark from Arbogast et al. (2017) to show that our formulation is correct, and that the solver performs much better than the previous one in Dannberg & Heister (2016). The benchmark specifically addresses the transition between regions with both melt and solid – where the coupled Stokes/Darcy systems is solved – and regions without melt – where the problem is reduced to the Stokes problem. This is done by choosing the porosity as zero in the upper half of the model domain, and as a quadratic function in the lower half, in such a way that the transition between the two regions is continuous and smooth (Figure 2). Under the assumption that $\phi \ll 1$, Arbogast et al. (2017, Equations 6.21–6.23) derive an approximate solution for this given porosity distribution, which we use to compute errors and convergence rates of our method.

Our numerical results show similar convergence rates as Arbogast et al. (2017): quadratic convergence for the solid velocity and linear convergence for the fluid and compaction pressure. Beyond that, we find that the number of linear solver iterations is not sensitive to problem size, and that the iteration count does not vary substantially in dependence of the material properties, such as, for example, the ratio between shear and compaction viscosity (Tables 2 and 3). This is a substantial improvement from the very strong dependence on both problem size and material properties exhibited by the method used in Dannberg & Heister (2016), which is what motivated the present study.

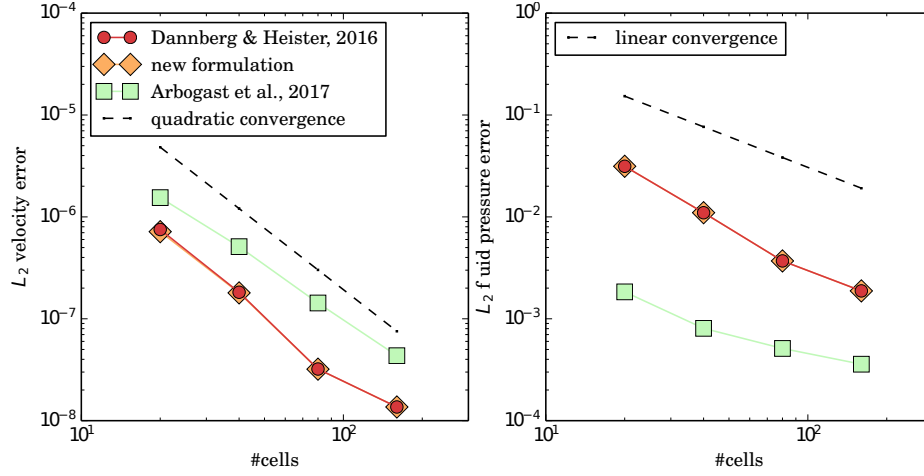


Figure 3. Error for solid velocity and fluid pressure. Results from Arbogast et al. (2017), Table 6 are plotted for comparison. For the method of Dannberg & Heister (2016), the linear solver does not converge for a resolution higher than $n = 80$, so the results shown are using a direct solver.

Problem size: Number of linear solver iterations

#cells	Dannberg & Heister (2016)	this study
20	107	5
40	303	7
80	820	10
160	no convergence	8

Table 2. Iteration count in dependence of the problem size. While for the method of Dannberg & Heister (2016) the number of iterations increases with the number of degrees of freedom, our new method needs fewer iterations and the iteration count is independent of the problem size.

Parameters variations: Number of linear solver iterations

ξ_{\max}/η	Dannberg & Heister (2016)	this study
10^1	24	11
10^2	63	12
10^3	214	14
10^4	820	16
10^5	no convergence	16
10^6	no convergence	16
10^7	no convergence	11

Table 3. Iteration count in dependence of the bulk-to-shear-viscosity ratio, for $n = 80$ cells in vertical direction.

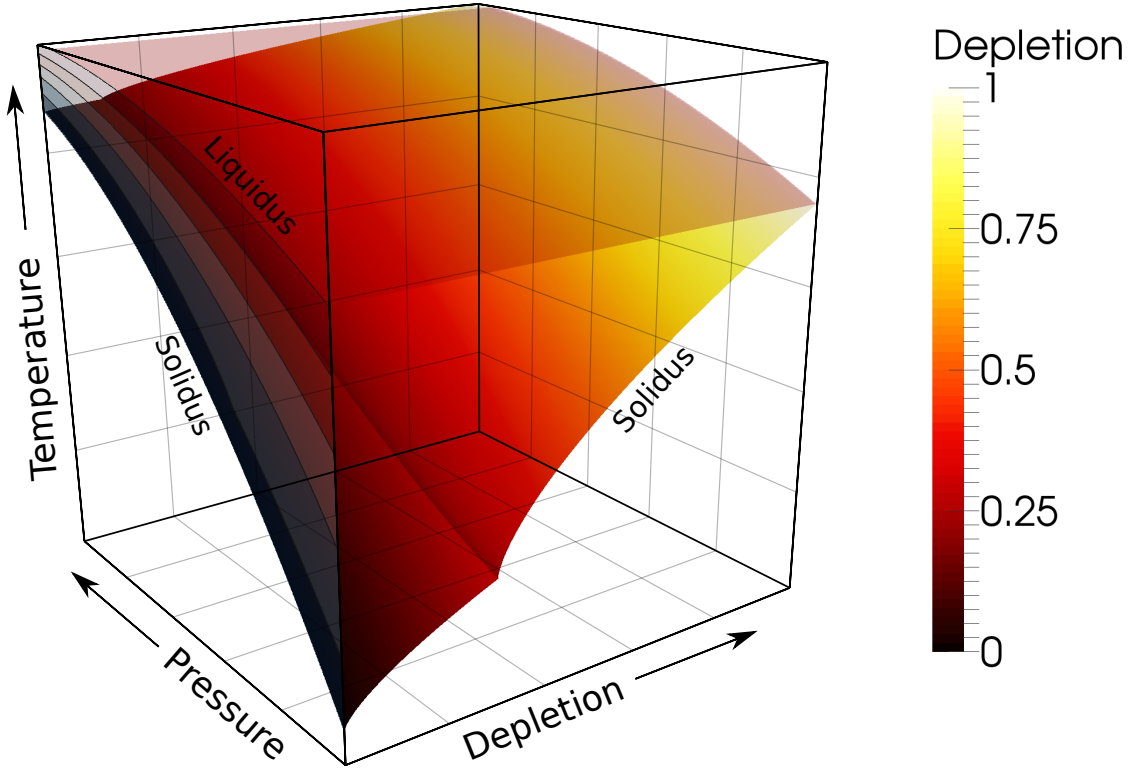


Figure 4. Melting parametrization from Katz et al. (2003). Shown is a temperature range from 1300 to 2300 K and a pressure range from 0 to 10 GPa. The kink signifies the exhaustion of clinopyroxene in the host rock. Contours between solidus and liquidus in the temperature–pressure plane are drawn at melt fractions of 0%, 20%, 40%, 60%, 80%, and 100%.

3.2 Numerical results: 2-D mid-ocean ridge model

In the previous section we have shown that our formulation correctly reproduces analytical solutions and solver performance is independent of problem size and contrast between shear and compaction viscosity. In the following, we will demonstrate that our implementation also performs well for realistic models of coupled magma/mantle dynamics that are relevant for advancing our understanding of how magma rises from its source region to the surface. For this purpose, we set up a mid-ocean ridge model with a visco-plastic, temperature and porosity-dependent rheology. Prescribed outflow at the side boundaries leads to corner flow within the domain, so that inflowing material rises and melts adiabatically below the ridge. We use the melting parametrization from Katz et al. (2003) as depicted in Figure 4. To track the temperature, the porosity and the degree of melting (depletion), we use second-order finite elements and advect them as fields, employing an entropy-viscosity stabilization (Guermond et al. 2011).

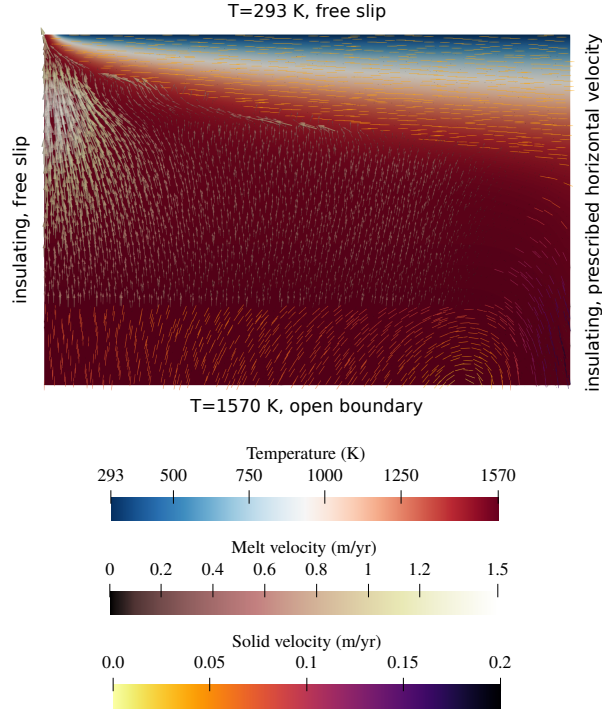


Figure 5. Setup of the mid-ocean ridge model. Arrows mark the melt velocity and lines illustrate the direction of the solid velocity.

3.2.1 Boundary conditions

The temperature is fixed to 293 K at the top boundary and to 1570 K at the bottom boundary, while the side boundaries are insulating. Porosity and depletion fields are fixed to zero at the inflow (bottom) boundary, and Neumann boundary conditions are applied at the other boundaries. We prescribe the horizontal component of the velocity to a constant value of 4 cm/yr on the right model boundary to generate the corner flow that is typical for mid-ocean ridges. In addition, the lithostatic pressure is applied as a traction boundary condition for the vertical stress component at the right boundary and the stress at the bottom boundary, allowing free in and outflow. The top and left boundaries are free-slip boundaries and are impermeable to flow. Figure 5 illustrates the setup.

To allow melt to escape at the ridge axis, we add a temperature perturbation to the otherwise constant boundary temperature at the top of the model in form of a hyperbolic tangent close to the ridge axis. So the total boundary temperature is defined as

$$T = T_0 + \Delta T \left(1 - \tanh \left(\frac{x - x_0}{w} \right) \right), \quad (13)$$

with $T_0 = 293$ K, $\Delta T = 600$ K, $x_0 = 2000$ m and $w = 1000$ m. This leads to a nonzero melt fraction at the ridge axis, where melt can flow out of the model domain. To avoid a suction effect at the ridge

axis, we prescribe the fluid pressure gradient at the upper model boundary as

$$\nabla p_f = (f\rho_f + (1-f)\rho_s)\mathbf{g}, \quad (14)$$

similarly to the pressure boundary condition applied in Katz (2010) for the same reason. In this expression, f controls the resistance to flow through the boundary: $f = 0$ would allow free outflow of melt like at an open boundary, and $f = 1$ corresponds to a closed boundary. Here we use $f = 0.99$, which is large enough to let melt flow out of the domain and limit the steady-state porosity beneath the ridge axis to approximately 10%, but not so large that the outflow dominates the melt flow in the whole melting region.

3.2.2 Material properties

We combine a temperature and porosity-dependent diffusion creep rheology with a stress limiter of the following form:

$$\eta(\phi, T) = \begin{cases} \eta_0 e^{-\alpha\phi - \beta(T-T_0)/T_0}, & \text{if } \sigma < \sigma_{yield} \\ \frac{\sigma_{yield}}{2\dot{\epsilon}_{II}} & \text{otherwise} \end{cases} \quad (15)$$

where $\dot{\epsilon}_{II}$ is the second invariant of the strain rate, and $\sigma_{yield} = C \cos(\phi_\eta) + p_s \sin(\phi_\eta)$ with the cohesion C and the friction angle ϕ_η . This way, the stress will not exceed the yield strength of the material, and deformation is localized at the ridge axis. The compaction viscosity is given as

$$\xi(\phi, T) = \xi_0 \frac{\phi_0}{\phi} e^{-\beta(T-T_0)/T_0}, \quad (16)$$

with the reference porosity $\phi_0 = 0.05$.

Most other material properties are chosen as in the mid-ocean ridge model in Katz (2010). The model is incompressible, so that the density is given as

$$\rho = [(\rho_s + \Delta\rho_C F)(1 - \phi) + \rho_f \phi] (1 - \alpha_{\text{thermal}}(T - T_{\text{ref}})), \quad (17)$$

where F is the degree of melting (depletion), $\Delta\rho_C$ is the density change due to depletion, and α_{thermal} is the thermal expansivity. A complete list of input parameters is given in Table 4.

3.2.3 Initial conditions

We first run a time-dependent model to generate realistic temperature, composition and porosity distributions for our scaling tests, which are instantaneous.

To prescribe initial conditions for the temperature and composition in the time-dependent model, we use a temperature distribution based on the half-space cooling model to compute the equilibrium

Table 4. Parameters used for the mid-ocean ridge models.

Quantity	Value
Reference bulk viscosity ξ_0	$4 \cdot 10^{20}$ Pa s
Reference shear viscosity η_0	10^{18} Pa s
Melt viscosity η_f	1 Pa s
Solid density ρ_s	3000 kg/m^3
Fluid density ρ_f	2500 kg/m^3
Compositional density contrast $\Delta\rho_C$	500 kg/m^3
Reference permeability k_0	10^{-7} m^2
Reference porosity ϕ_0	0.05
Melt weakening parameter α	27
Temperature weakening parameter β	24
Thermal expansivity α_{thermal}	$2 \times 10^{-5} \text{ 1/K}$
Specific heat C_p	1250 J/(kg K)
Reference temperature T_{ref}	1600 K
Thermal conductivity k_{thermal}	4.7 W/(m K)
Cohesion C	$2 \cdot 10^7 \text{ Pa}$
Friction angle ϕ_η	30°
X extent	105 km
Z extent	70 km

melt fraction everywhere in the domain. As we take into account latent heat effects, this initial temperature is reduced in dependence of the amount of melting, and we find the solution iteratively. The resulting temperature is prescribed as initial temperature, and the resulting melt fraction is prescribed as initial depletion. The porosity is assumed to be zero everywhere in the domain at the model start. We first let the model run in a low resolution of 1 km for 3 million years to produce a more realistic temperature and compositional structure that takes into account the dynamic effects of melt transport. Then we increase the resolution to 550 m throughout the model domain and 270 m within a distance of 7 km around the ridge axis, where melt is extracted from the domain. On this finer mesh, we compute another 3 million years of model evolution, which is approximately the time it takes for material to cross the distance from the ridge axis to the far end of the model domain. Finally, we let the model evolve for another 8000 years (~ 370 time steps) with a uniform cell size of 140 m. This allows us to export the final state of the model to data files and use them to create high-resolution initial conditions for the model runs presented in the following. The data files are freely available at <https://github.com/tjhei/paper-aspect-melt-paper-2-data> together with the input files and allow it to reproduce our results.

Problem size: Number of linear solver iterations

#cells	GMRES iterations	average S block iterations
6, 144	213	157
24, 576	176	199
98, 304	118	229
393, 216	118	261
1, 572, 864	116	308
6, 291, 456	119	343

Table 5. Iteration counts for a linear solver tolerance of 10^{-14} .

3.2.4 Influence of problem size

To show that iteration numbers of the linear solver do not vary substantially with the size of the problem we are solving, we used the data files created from the final state of the 2-D mid-ocean ridge model described above to compute instantaneous flow models with different resolutions. Our results (see Table 5) show that the number of GMRES iterations is insensitive to the problem size, and the number of Schur complement iterations that are done per GMRES iteration only increases slightly with problem size. This result highlights the usefulness of our new method for large-scale magma/mantle dynamics models.

3.2.5 Influence of material properties

Rhebergen et al. (2014) and Rhebergen et al. (2015) have identified the ratio of compaction to shear viscosity as a key control on the rate of convergence of the iterative solver for the linear system we solve. Because the compaction viscosity is inversely proportional to the porosity, this ratio increases with decreasing porosity and becomes infinity in the limit of $\phi \rightarrow 0$ (which is the mathematically degenerate case) at the boundaries between regions with and without melt.

As this boundary is present in most models of magma/mantle dynamics, and has the potential to slow down convergence of the linear solver substantially, we investigate the dependence of the convergence rate on the compaction-to-shear-viscosity ratio. In our new formulation, we address the part of the problem that relates to the interface between the solid and the partially molten region by rescaling the equation that contains the compaction viscosity, and introducing a threshold for the onset of two-phase flow. Hence, in the following we will test the sensitivity of the iteration count to both the global compaction-to-shear-viscosity ratio and the choice of the melt transport threshold.

For this purpose, we use the same setup as described above in section 3.2.4 to compute instantaneous flow models. When the compaction-to-shear-viscosity ratio ξ/η is varied globally (Table 6),

Compaction-to-shear-viscosity ratio: Number of linear solver iterations

ξ/η ($\phi = 1.5\%$)	GMRES iterations	average S block iterations
$2 \cdot 10^1$	74	116
$2 \cdot 10^2$	124	147
$2 \cdot 10^3$	124	248
$2 \cdot 10^4$	125	345
$2 \cdot 10^5$	175	403
$2 \cdot 10^6$	182	434
$2 \cdot 10^7$	183	435

Table 6. Iteration counts for a linear solver tolerance of 10^{-14} , and 887939 Stokes degrees of freedom (98304 mesh cells).

we see that there is a weak dependence of the GMRES iteration count on the compaction-to-shear-viscosity ratio, similarly to the results of Rhebergen et al. (2015). In addition, the S block iteration count increases with ξ/η . This is expected, as our formulation only addresses the increase of ξ as the porosity $\phi \rightarrow 0$. However, this sensitivity to ξ/η might not be problematic for realistic applications, as this ratio is expected to be on the order of 1–100 (Hewitt & Fowler 2008; Takei & Holtzman 2009; Simpson et al. 2010; Katz 2010; Schmeling et al. 2012; Alisic et al. 2014).

Note that the values ξ/η given in Table 6 correspond to the ratio of the shear and compaction viscosity for a porosity $\phi = 0.015$. The actual ratio in the model varies by two orders of magnitude upwards from this reference value due to the different dependencies on porosity, which means that the ratio increases both for very low and very high porosities.

In addition, we also test the sensitivity of the solver convergence rate to the increase in the compaction-to-shear-viscosity ratio as $\phi \rightarrow 0$ by varying the threshold for the onset of two-phase flow. The results (Table 7) reveal no sensitivity of the GMRES iteration count and only a very weak sensitivity of the S block iteration count to this threshold.

Threshold for melt transport: Number of linear solver iterations

$K_{\text{threshold}}$	GMRES iterations	average S block iterations
10^{-6}	124	248
10^{-8}	124	252
10^{-10}	124	255
10^{-12}	124	262
10^{-14}	124	290

Table 7. Iteration counts for a linear solver tolerance of 10^{-14} , and 887939 Stokes degrees of freedom (98304 mesh cells).

Threshold for melt transport: Number of linear solver iterations

		Dannberg & Heister (2016)		this study	
$K_{\text{threshold}}$	$\phi_{\text{threshold}}$	GMRES iterations	avg. S block iterations	GMRES iterations	avg. S block iterations
10^0	10^{-2}	1496	10	62	30
10^{-1}	$2.15 \cdot 10^{-3}$	3471	10	63	110
10^{-2}	$4.64 \cdot 10^{-4}$	12600	10	64	137
10^{-3}	10^{-4}	42272	10	64	166
10^{-4}	$2.15 \cdot 10^{-5}$	95869	10	64	166
10^{-5}	$4.64 \cdot 10^{-6}$	–	–	64	173

Table 8. Iteration counts for a linear solver tolerance of 10^{-8} , and 62404 Stokes degrees of freedom (6144 mesh cells). Entries marked with ‘–’ indicate that there was no convergence reached after 100000 GMRES iterations.

Finally, we also want to provide a direct comparison to the method of Dannberg & Heister (2016). Due to the strong dependence on problem size, we had to reduce the resolution, increase the threshold for the onset of two-phase flow and increase the solver tolerance of the model for this comparison, and we also removed the temperature dependence of viscosity. The results in Table 8 show both overall lower iteration counts and lower sensitivity to model parameters for the formulation developed in this study. They highlight that also for realistic application cases such as melt migration below mid-ocean ridges, our new method performs substantially better than the one developed in Dannberg & Heister (2016), and is feasible for accurately modelling the interface between regions with and without melt.

3.2.6 Scaling behaviour of the implemented solver

In practice, not only the number of iterations, but also the wallclock time per iteration controls the computational cost of a model time step. Therefore we present scaling tests for the models of this section and Section 3.3 in Figure 6. All scaling tests were done on Intel Xeon (Skylake) cores connected by an Intel Omnipath network at the Stampede 2 system of the Texas Advanced Computing Center (TACC).

Both models show a linear strong scaling to about 50,000 degrees of freedom (DoFs) per core (considering only solid velocity, fluid pressure, and compaction pressure DoFs); beyond that the efficiency drops significantly. The weak scaling results suggest a slightly less than optimal, but still acceptable scaling with model size, which leads to an increase of Stokes solver time by about a factor of 2.7 when increasing the model size by a factor of 64 (from 5 million DoFs to 327 million DoFs in 2-D, and from 6 million DoFs to 396 million DoFs in 3-D). These results are consistent with the slight increase in Schur complement iterations with model size discussed in Section 3.2.4 and show that our

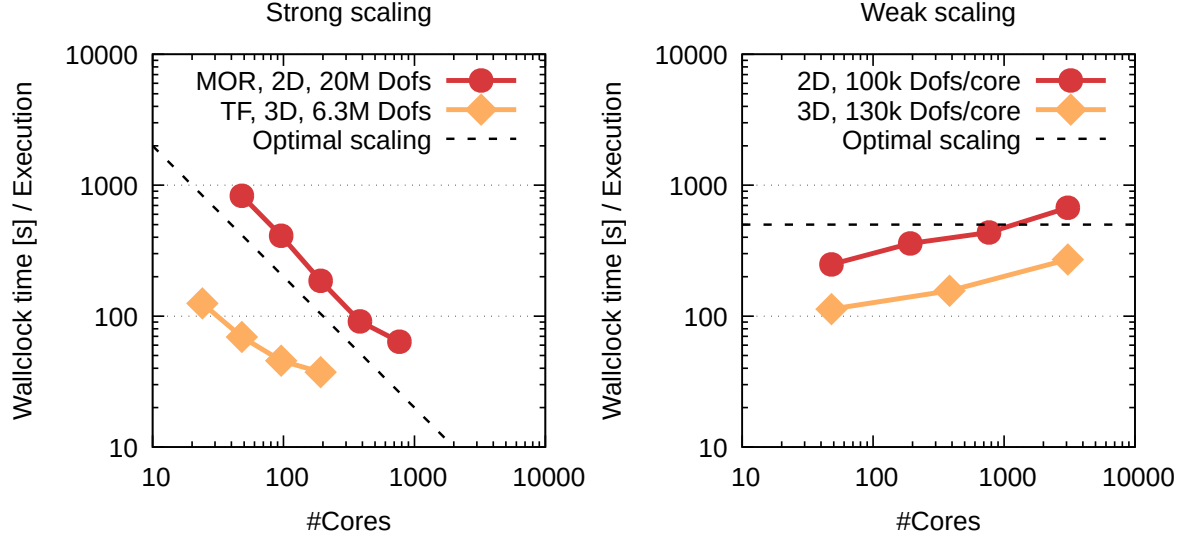


Figure 6. Strong and weak scaling results for the 2-D mid-ocean ridge (MOR) model described in Section 3.2 and the 3-D transform fault (TF) model described in Section 3.3. The presented values represent the time required for solving the combined Stokes/Darcy equations once (i.e. without time spent for assembly, and equations for temperature, composition, and porosity). Note that the two model series use different iterative solver tolerances and values for $K_{\text{threshold}}$ so that absolute wallclock times cannot be compared between 2-D and 3-D. The scaling behaviour is not affected by these choices.

solver scales reasonably well to problem sizes of several hundred million and potentially a few billion degrees of freedom, although there is still room for optimization.

3.2.7 A note on mesh refinement

In Dannberg & Heister (2016), we discussed some strategies for adaptively refining the mesh in models with coupled magma/mantle dynamics. They mainly focused on refining the mesh based on solution variables or material properties. However, one can think of other useful mesh refinement strategies: One alternative is to just refine all cells where melt is present. Another natural criterion that comes to mind is the intrinsic length scale of melt migration: the compaction length. The compaction length is defined as $\delta_c = \sqrt{(\xi + 4\eta/3)K_D}$ and is the length scale over which the compaction pressure responds to variations in fluid flux (Spiegelman et al. 2007; McKenzie 1984; Spiegelman 1993). Hence, this length scale should be well resolved in numerical models that consider the compaction of partially molten rock. As the compaction length varies spatially and temporally, depending on the porosity of

the rock and the material properties, adaptive mesh refinement can be a useful tool to make sure that the compaction length is resolved in an evolving model, while simultaneously saving computational resources by coarsening the mesh in regions with a larger compaction length.

We implemented both mesh refinement strategies: One that refines all ‘melt cells’, and one that adapts the size of the grid cells depending on the local compaction length, allowing it to define the minimum number of cells per compaction length that should be present in the model. However, it becomes apparent that both of these strategies are inferior to refining based on solution variables, at least if the model output of interest is directly related to the solution variables (Figure 8). Refining in ‘melt cells’ performs slightly better than global refinement, but not nearly as good as refining based on the porosity or the melt velocity, and using the compaction length as a refinement criterion is inferior even to refining globally. The reason for that is that the compaction length decreases with increasing melt fraction, which means that the mesh is refined first at the boundaries of the melting region. This increases the number of degrees of freedom, but does not accurately resolve the melt flux in regions where the porosity is large.

The compaction length can still be a useful criterion to estimate the length scales of features emerging in a two-phase flow model, which can be used to set a minimum resolution in the partially molten regions. In our mid-ocean ridge models, the compaction length (assuming a reference porosity of 0.5%) is on the order of 10 km, which is well resolved in all models in Figure 8, as the coarsest resolution is 2 km. Nevertheless, locally, features may be substantially smaller than the compaction length, and our models require a global resolution of 140 m to reach an error of 1% for the global melt flux, which corresponds to ~ 70 mesh cells per compaction length. This suggests that just resolving the compaction length might not be sufficient for accurately modelling of two-phase flow.

3.3 3-D Application: Oceanic transform fault

To show the capability of our method to solve large-scale 3-D problems of coupled magma/mantle dynamics, we present an instantaneous mid-ocean ridge model that includes two ridge segments offset by a transform fault. We generated the initial conditions for this setup from the end state of the two-dimensional mid-ocean ridge model by mirroring the distribution of temperature, depletion and porosity with respect to the ridge axis and extending it uniformly in the third dimension, except for an offset of the ridge axis of 40 km in the center of the model. The material properties and boundary conditions are identical to the 2-D model described in Section 3.2, and the new model boundaries at the front and back are free slip boundaries. The model extents are $170 \times 170 \times 70$ km, and we solve the (time-independent) coupled Stokes/Darcy equations on approximately 8.9 million cells (262 million degrees of freedom combined for solid velocity, fluid pressure and compaction pressure), as visualized

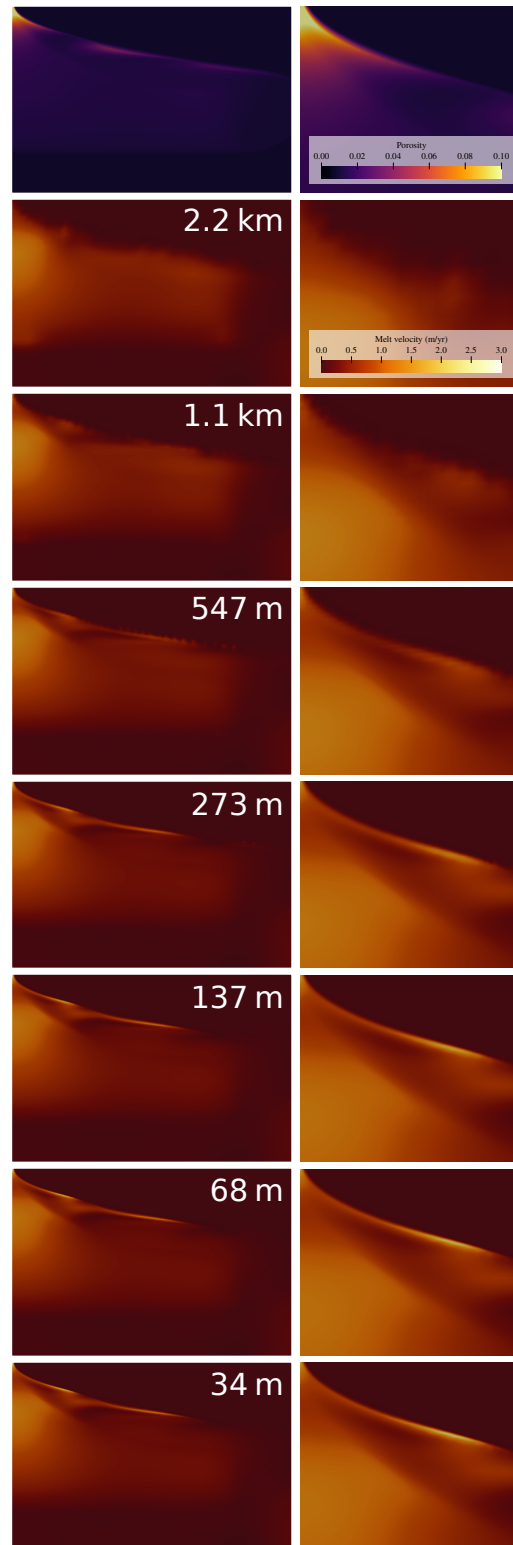


Figure 7. Porosity (top row) and melt velocity (all rows below) in a 2-D mid-ocean ridge model for different resolutions as given in Table 5. The left column shows the whole model, the right column shows the part of the model closest to the ridge axis. Resolution increases from top to bottom, as specified by the white labels indicating the cell size in each model.

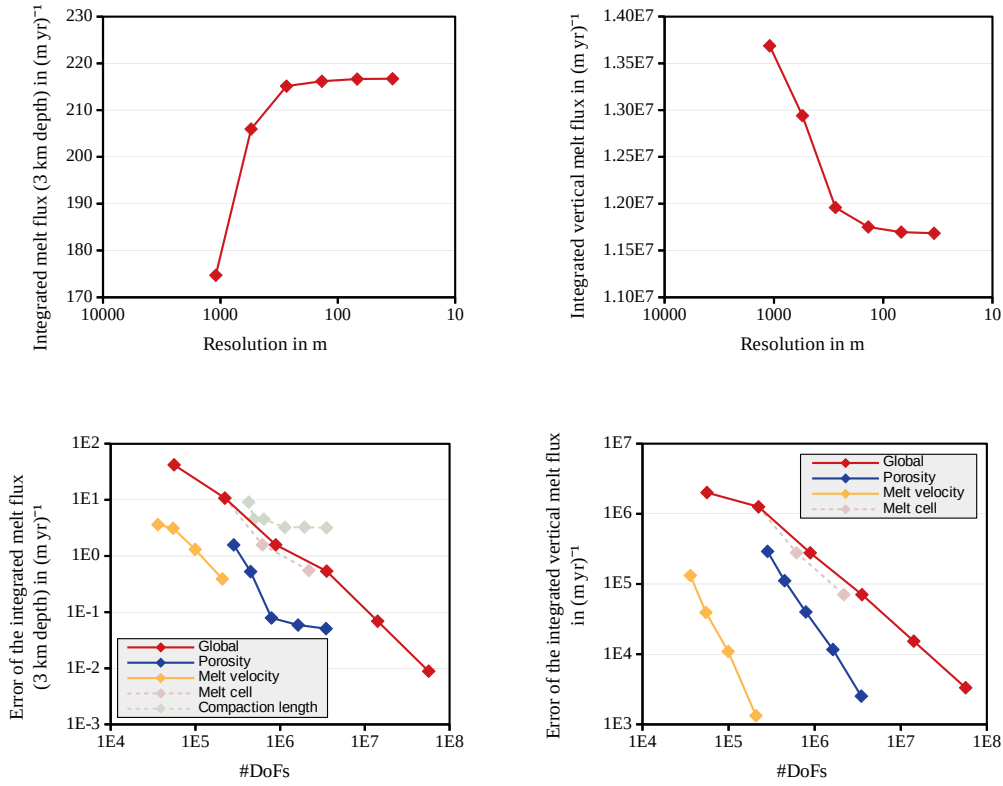


Figure 8. Melt flux in a 2-D mid-ocean ridge model for different resolutions. The top row shows the vertical melt flux integrated over a horizontal line in 3 km depth (left) and the vertical melt flux integrated over the whole model domain (right) for models with uniform refinement of the mesh. The bottom row panels feature the same quantities as the corresponding panels above, only that they show the error from the Richardson extrapolation of the data in the top row in logarithmic scale. The different data series represent uniform mesh refinement (red), and adaptive mesh refinement based on the porosity (blue) and the melt velocity (yellow), both using the Kelly error estimator, the presence of melt (light red) and the compaction length (light green). The results show that using adaptive mesh refinement can yield the same accuracy while using 1-2 orders of magnitude fewer degrees of freedom, and that for globally integrated quantities like the integrated melt flux, it can also yield a higher order of convergence.

in Figure 1. We make use of adaptive mesh refinement to increase the resolution in areas where melt is present, resulting in a cell size of approximately 550 m.

The model output is illustrated in Figure 9, and shows that even though the temperature and porosity fields are symmetric with respect to the ridge axis of the individual ridge segments, the flow field evinces three-dimensional structures. Melt is focused towards the ridge axis of the opposite ridge segment if that one is closer than the axis of the ridge segment the melt was generated at. Hence, melt crosses the transform fault, and the melt flux along the ridge axis decreases with increasing

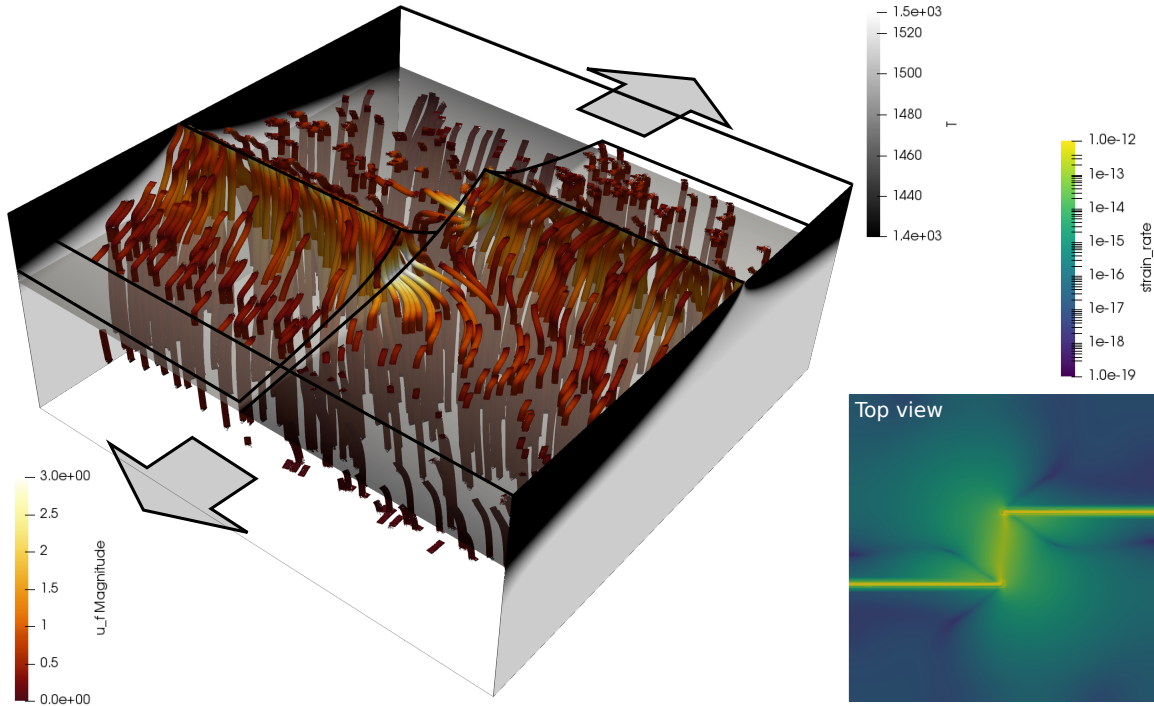


Figure 9. Visualization of a three-dimensional model of two mid-ocean ridge segments separated by a transform fault. Red-to-yellow streamlines show the melt velocity, highlighting the three-dimensional structure of the flow field (curved yellow–white streamlines cross the transform fault). Black-to-white background colours indicate temperature and grey arrows illustrate the prescribed spreading direction. The inset shows the deformation at the surface of the model.

distance from the fault. In addition, deformation is not only localized at the two ridge segments, but the employed stress-limiter rheology also leads to localization at the transform fault, where no melt is reaching the surface. It is clear that individual features of the flow field are likely to be different in a model with time evolution, where melt pathways are influenced by the acting stresses. However, our results highlight that high-resolution time-dependent three-dimensional models have a large potential to advance our understanding of the influence of transform faults and oblique spreading directions on the focusing of melt towards the ridge axis, and it is feasible to compute such models with the formulation we developed here.

4 CONCLUSIONS

We have developed a new formulation of the governing equations of magma/mantle dynamics that allows it to accurately model the problem, even in the case of vanishing porosity and large ratios of compaction and shear viscosity. We achieve this by rescaling one of the solution variables, the compaction pressure, with the square root of the Darcy coefficient, and constraining the compaction

pressure degrees of freedom to zero for very small porosities. This makes the linear system well-posed, even for small or vanishing porosities.

Our numerical results show that the number of linear solver iterations is independent of the problem size, and that there is only a mild sensitivity to the model parameters. Hence, the method can be applied throughout a wide parameter range. Scaling tests reveal that our solver scales reasonably well to problem sizes of several hundred million, and potentially up to a few billion degrees of freedom. Most importantly, the solver convergence does not change with decreasing porosity, when the interface between solid and partially molten regions is approached.

Finally, we demonstrated that our new formulation is suitable for modelling large-scale realistic problems of magma/mantle dynamics, such as melt generation and transport beneath mid-ocean ridges. Hence, we are confident that our new formulation and its implementation in the open source geodynamic modelling software ASPECT will prove most valuable for exploring the the interactions of solid rock deformation and melt generation and transport in three dimensions.

5 ACKNOWLEDGEMENTS

The authors would like to thank the Isaac Newton Institute for Mathematical Sciences, Cambridge, for support and hospitality during the programme Melt in the Mantle, which facilitated many fruitful discussions that lead to the idea for this paper.

All authors were partially supported by the Computational Infrastructure for Geodynamics initiative (CIG), through the National Science Foundation under Awards No. EAR-0949446 and EAR-1550901, administered by The University of California-Davis. TH was partially supported by the National Science Foundation awards DMS-1522191, DMS-1820958, OAC-1835452 and by Technical Data Analysis, Inc. through US Navy SBIR N16A-T003. JD and RG were partially supported by the National Science Foundation under award OCI-1148116 as part of the Software Infrastructure for Sustained Innovation (SI2) program. JD gratefully acknowledges the support of the Deep Carbon Observatory. The authors acknowledge the Texas Advanced Computing Center (TACC, <http://www.tacc.utexas.edu>) at The University of Texas at Austin for providing high-performance computing resources that have contributed to the research results reported within this paper. Clemson University is acknowledged for generous allotment of compute time on the Palmetto cluster.

The authors greatly appreciate all of these sources of support.

REFERENCES

- Alisic, L., Rudge, J. F., Katz, R. F., Wells, G. N., & Rhebergen, S., 2014. Compaction around a rigid, circular inclusion in partially molten rock, *Journal of Geophysical Research: Solid Earth*, **119**(7), 5903–5920.
- Alzetta, G., Arndt, D., Bangerth, W., Boddu, V., Brands, B., Davydov, D., Gassmoeller, R., Heister, T., Heltai, L., Kormann, K., Kronbichler, M., Maier, M., Pelteret, J.-P., Turcksin, B., & Wells, D., 2018, accepted. The deal.II library, version 9.0, *Journal of Numerical Mathematics*.
- Arbogast, T., Hesse, M. A., & Taicher, A. L., 2017. Mixed methods for two-phase darcy–stokes mixtures of partially melted materials with regions of zero porosity, *SIAM Journal on Scientific Computing*, **39**(2), B375–B402.
- Bangerth, W., Hartmann, R., & Kanschat, G., 2007. deal.II – a general purpose object oriented finite element library, *ACM Trans. Math. Softw.*, **33**(4), 24/1–24/27.
- Bangerth, W., Dannberg, J., Gassmoeller, R., & Heister, T., 2018a. ASPECT v2.0.0 [software].
- Bangerth, W., Dannberg, J., Gassmöller, R., Heister, T., et al., 2018b. ASPECT: *Advanced Solver for Problems in Earth’s ConvecTion*, User Manual, Davis, CA.
- Butler, S., 2017. Shear-induced porosity bands in a compacting porous medium with damage rheology, *Physics of the Earth and Planetary Interiors*, **264**, 7–17.
- Cheadle, M., Elliott, M., & McKenzie, D., 2004. Percolation threshold and permeability of crystallizing igneous rocks: The importance of textural equilibrium, *Geology*, **32**(9), 757–760.
- Dannberg, J. & Heister, T., 2016. Compressible magma/mantle dynamics: 3-d, adaptive simulations in aspect, *Geophysical Journal International*, **207**(3), 1343–1366.
- Grove, R. R., 2017. *Discretizations & Efficient Linear Solvers for Problems Related to Fluid Flow*, Ph.D. thesis, Clemson University.
- Guermond, J.-L., Pasquetti, R., & Popov, B., 2011. Entropy viscosity method for nonlinear conservation laws, *J. Comput. Phys.*, **230**, 4248–4267.
- Heister, T., Dannberg, J., Gassmöller, R., & Bangerth, W., 2017. High accuracy mantle convection simulation through modern numerical methods–ii: realistic models and problems, *Geophysical Journal International*, **210**(2), 833–851.
- Hewitt, I. & Fowler, A., 2008. Partial melting in an upwelling mantle column, in *Proceedings of the Royal Society of London A: Mathematical, Physical and Engineering Sciences*, vol. 464, pp. 2467–2491, The Royal Society.
- Katz, R. F., 2006. The dynamics of melt and shear localization in partially molten aggregates, *Nature*, **442**, 676–679.
- Katz, R. F., 2008. Magma dynamics with the enthalpy method: Benchmark solutions and magmatic focusing at mid-ocean ridges, *Journal of Petrology*, **49**(12), 2099–2121.
- Katz, R. F., 2010. Porosity-driven convection and asymmetry beneath mid-ocean ridges, *Geochemistry, Geophysics, Geosystems*, **11**(11), Q0AC07.
- Katz, R. F., Spiegelman, M., & Langmuir, C. H., 2003. A new parameterization of hydrous mantle melting,

- Geochemistry, Geophysics, Geosystems*, **4**(9), 1073.
- Katz, R. F., May, D., Rees Jones, D., & Tian, M., 2017. The subduction framework utilising scientific computing (subfusc)-an open-source simulation tool for two-phase dynamics of subduction zones, in *AGU Fall Meeting Abstracts*.
- Keller, T., May, D. A., & Kaus, B. J. P., 2013. Numerical modelling of magma dynamics coupled to tectonic deformation of lithosphere and crust, *Geophysical Journal International*, **195**(3), 1406–1442.
- Keller, T., Katz, R. F., & Hirschmann, M. M., 2017. Volatiles beneath mid-ocean ridges: Deep melting, channelised transport, focusing, and metasomatism, *Earth and Planetary Science Letters*, **464**, 55–68.
- McKenzie, D., 1984. The generation and compaction of partially molten rock, *Journal of Petrology*, **25**(3), 713–765.
- Rhebergen, S., Wells, G. N., Katz, R. F., & Wathen, A. J., 2014. Analysis of block preconditioners for models of coupled magma/mantle dynamics, *SIAM Journal on Scientific Computing*, **36**(4), A1960–A1977.
- Rhebergen, S., Wells, G. N., Wathen, A. J., & Katz, R. F., 2015. Three-field block preconditioners for models of coupled magma/mantle dynamics, *SIAM Journal on Scientific Computing*, **37**(5), A2270–A2294.
- Schmeling, H., Kruse, J. P., & Richard, G., 2012. Effective shear and bulk viscosity of partially molten rock based on elastic moduli theory of a fluid filled poroelastic medium, *Geophysical Journal International*, **190**(3), 1571–1578.
- Simpson, G., Spiegelman, M., & Weinstein, M. I., 2010. A multiscale model of partial melts: 1. effective equations, *Journal of Geophysical Research: Solid Earth*, **115**(B4).
- Spiegelman, M., 1993. Flow in deformable porous media. part 1 simple analysis, *Journal of Fluid Mechanics*, **247**, 17–38.
- Spiegelman, M., Katz, R., & Simpson, G., 2007. An introduction and tutorial to the “McKenzie Equations” for magma migration, *Preprint, Columbia University, Dept. of Applied Physics and Applied Mathematics*.
- Takei, Y. & Holtzman, B. K., 2009. Viscous constitutive relations of solid-liquid composites in terms of grain boundary contiguity: 1. grain boundary diffusion control model, *Journal of Geophysical Research: Solid Earth*, **114**(B6).
- Turner, A. J., Katz, R. F., Behn, M. D., & Keller, T., 2017. Magmatic focusing to mid-ocean ridges: The role of grain-size variability and non-newtonian viscosity, *Geochemistry, Geophysics, Geosystems*, **18**(12), 4342–4355.
- Weatherley, S. M. & Katz, R. F., 2012. Melting and channelized magmatic flow in chemically heterogeneous, upwelling mantle, *Geochemistry, Geophysics, Geosystems*, **13**(5), Q0AC18.
- Wilson, C. R., Spiegelman, M., van Keken, P. E., & Hacker, B. R., 2014. Fluid flow in subduction zones: The role of solid rheology and compaction pressure, *Earth and Planetary Science Letters*, **401**, 261–274.
- Zhu, W. & Hirth, G., 2003. A network model for permeability in partially molten rocks, *Earth and Planetary Science Letters*, **212**(3-4), 407–416.